

A Polarized Reflection and Material Dataset of Real World Objects

Jing Yang, Krithika Dharanikota, Emily Jia, Haiwei Chen, Yajie Zhao
 Institute for Creative Technologies, University of Southern California
 {jyang, kdharanikota, ejia, chenh, zhao}@ict.usc.edu

Abstract

Accurately modeling how real-world materials reflect light remains a core challenge in inverse rendering, largely due to the scarcity of real measured reflectance data. Existing approaches rely heavily on synthetic datasets with simplified illumination and limited material realism, preventing models from generalizing to real-world images. We introduce a large-scale polarized reflection and material dataset of real-world objects, captured with an 8-camera, 346-light Light Stage equipped with cross/parallel polarization. Our dataset spans 218 everyday objects across five acquisition dimensions—multiview, multi-illumination, polarization, reflectance separation, and material attributes—yielding over 1.2M high-resolution images with diffuse-specular separation and analytically derived diffuse albedo, specular albedo, and surface normals. Using this dataset, we train and evaluate state-of-the-art inverse and forward rendering models on intrinsic decomposition, relighting, and sparse-view 3D reconstruction, demonstrating significant improvements in material separation, illumination fidelity, and geometric consistency. We hope that our work can establish a new foundation for physically grounded material understanding and enable real-world generalization beyond synthetic training regimes. Project page: jingyang-carl.github.io/ICTPolarReal

1. Introduction

Modeling how physical materials reflect light is a cornerstone that transforms our understanding of natural images. Typically, the image capturing process that intricately entangles geometry, light sources and material properties is considered non-invertible. However, past decades have seen extensive efforts from computer vision research to estimate intrinsic images from natural photos, a process known as intrinsic image decomposition [2] or inverse rendering [32]. While traditional methods towards this end had to rely on hand-crafted priors for estimation of low-order effects [8, 15, 34, 42], the quality of intrinsic image decomposition has been drastically improved in

recent years thanks to the emergence of dedicated synthetic datasets [12, 21, 23, 33] and large generative models [9, 11, 24, 27, 36, 40, 43].

The majority of improvements observed in recent intrinsic image decomposition models stem from synthetically rendered data. While CGI renderers can produce visually appealing images, they are constrained by simplified illumination models and limited material realism. Common shading models approximate bidirectional reflectance using analytical BRDFs or a small number of samples, ignoring multi-scattering, polarization, and subsurface transport that are ubiquitous in real objects. Moreover, few synthetic assets possess physically validated material parameters or polarization information, leading to discrepancies between rendered and real observations. Consequently, models trained exclusively on synthetic data often fail to generalize to uncontrolled lighting or real photographs. Recently, [30] collected the Multi-Illumination Dataset that provides real-life photos captured in different lighting conditions, but their lack of measurement for intrinsic decompositions limit their uses in training supervised image decomposition generative models.

In this paper, we tackle the challenges to collect a real-life reflection and material dataset, where we physically measured the surface reflectance of apples, bananas, cantaloupes, cabbages, onions, sweet potatoes, fabric bags, handbag logos, reusable bags, metal kettles, marbles, mirror balls, ceramic jars, glass bottles, plastic toys, rubber balls, wooden figurines, paper boxes, stone pots, and many more, covering a broad spectrum of material types including organic produce, plastics, rubbers, metals, ceramics, glass, fabrics, wood, paper, and other everyday household materials. By exploiting polarization, our system physically separates diffuse and specular reflections under controlled One-Light-at-a-Time (OLAT) illumination. Each object is observed from eight viewpoints and 346 lighting directions, yielding dense, polarization-separated reflectance fields. The dataset covers a diverse set of everyday objects, ranging from metals and ceramics to translucent and rough dielectrics, each captured with high dynamic range and geometric calibration. This results in the first real-life dataset

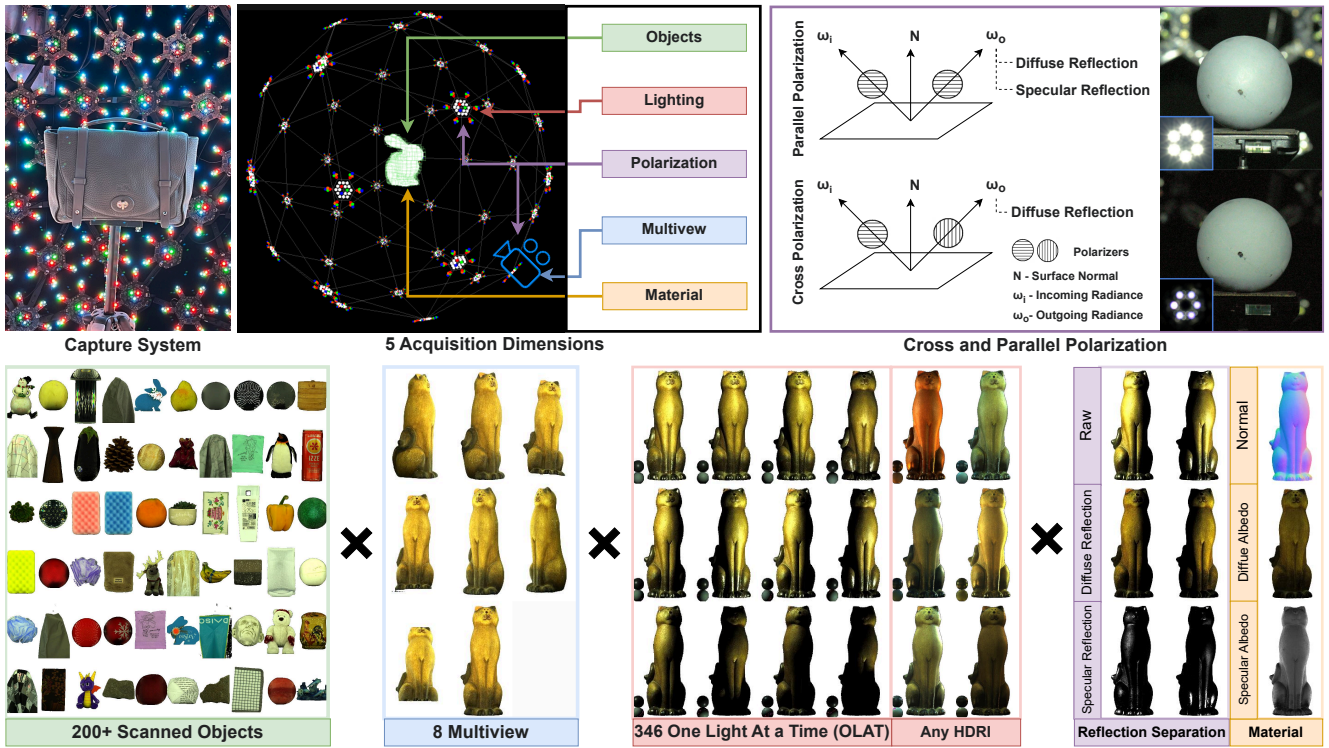


Figure 1. **Overview of our polarized reflection and material dataset.** Our Light Stage capture system records real-world objects under controlled lighting, polarization, and multiview conditions. The dataset spans five acquisition dimensions: objects, lighting, polarization, multiview, and material. Each object is captured under 346 One-Light-at-a-Time (OLAT) illuminations and can be synthesized into arbitrary HDRI lighting. Cross and parallel polarization enable reflection separation into diffuse and specular components, from which material attributes such as albedo and normal are derived, resulting in more than 1,200,000 (1.2 million) captured images at 6144x3240 resolution.

that can directly supervise deep neural networks that perform material decomposition and physically-based neural rendering.

To validate the effectiveness of our constructed dataset, we conduct comprehensive qualitative and quantitative evaluations of state-of-the-art techniques across multiple tasks, including intrinsic image decomposition, forward relighting, and sparse-view 3D reconstruction. These evaluations demonstrate that models trained or fine-tuned on our real-world measurements achieve markedly improved material separation, more faithful lighting response, and greater robustness to real-world appearance variations, capabilities that synthetic-only training cannot provide.

2. Related Works

2.1. Inverse Rendering

Originally proposed by [2], the inverse rendering problem, also known as intrinsic image decomposition, aims to separate an image into albedo, irradiance, and optionally, a specular component. Traditional methods address this problem by imposing prior assumptions on the different components, involving smooth shading [8, 15], grayscale shading [15, 42], albedo sparsity [3, 15, 29, 34], and others [7, 10]. Re-

cently, with the rapid development of deep learning, many studies have sought to learn such priors directly from data. Both supervised approaches [6, 14, 31, 35, 44] based on RGB renderings with ground-truth decompositions or annotations, and unsupervised methods [21, 38] using only multi-illumination images have been explored.

Many recent works have posed inverse rendering as an image-to-image translation problem that leverages rich priors from large image generation models [9, 11, 24, 27, 36, 40, 43]. While [4] has shown that an image generation model trained without any intrinsic image still can obtain implicit understanding of intrinsic image decomposition, many other works have relied on synthetic dataset that provides mapping from images to their decomposed components and mainly varied in the use of illumination representations (e.g. irradiance image in [40], HDR environment map in [24], Phong illumination model in [39]) and the selection and processing of synthetic datasets. In addition, large foundation models [16, 18] have specifically targeted the estimation of image depth and normal.

2.2. Dataset for Inverse Rendering

Due to the difficulty of measuring reflectance in real life, the majority of existing datasets are synthetically mod-

eled and rendered by computer graphics programs. Objaverse [12, 13] provides a large collection of 3D models, part of which contains materials that can be used to create intrinsic images. Hyperism [33], CGIntrinsic [21], OpenRooms [23], InvIndoor [22] and InteriorNet [20] are synthetic indoor scenes that provide ground truth material decomposition. Multi Illumination [30] provides real-life indoor photos under various illumination conditions with material annotations. However, the dataset is not suitable for direct supervision of inverse rendering models due to its lack of measurements for intrinsic images corresponding to the captured photos.

OpenSVBRDF [28] acquires 1000 spatially varying reflectance flat samples with an acquisition device, but the data is restricted to near-planar samples and only two viewpoints, limiting its applicability to full 3D objects and multi-view reconstruction. Open Illumination [25] instead focuses on illumination variation and captures only a small number of objects under a limited set of lighting patterns, providing valuable but narrow coverage of object and material diversity.

3. Dataset

We target the acquisition of **real-world, everyday objects** spanning a wide range of materials such as metals, ceramics, plastics, fabrics, wood, leather, glass, and translucent organics. In order to disentangle diffuse and specular reflections, each object is captured as a multi-view, polarized reflectance field that records how light interacts with the surface under hundreds of controlled illumination directions. From these measurements, we derive physically interpretable quantities including diffuse and specular reflection components, surface normal, and material albedo. This dataset provides the foundation for learning and evaluating physically grounded appearance models under real-world conditions. Examples are shown in Figure 1.

3.1. Capture System

The capture system consists of 346 LED light sources mounted on a geodesic dome and 8 synchronized RED Komodo 6K global shutter cameras positioned to cover a broad angular range. Each LED is equipped with either a cross- or parallel-oriented linear polarizer arranged in a hexagonal tiling pattern. The cameras are also equipped with rotatable linear polarizers, enabling consistent acquisition of polarized reflectance. For each lighting direction, we acquire two polarized observations per view: one under cross-polarized lighting and one under parallel-polarized lighting. This configuration enables per-light, per-view separation of diffuse and specular reflections via linear polarization analysis. Lights are triggered in a spiral order, **One Light At A Time (OLAT)**, from the frontal to the back hemisphere to ensure angularly uniform coverage. The full sequence con-

sists of 346 lighting conditions captured across 8 viewpoints at 6144×3240 resolution for each polarization status.

3.2. Acquisition

Our data acquisition consists of two stages: (1) polarized image capture and (2) material processing. The first stage records polarization-separated reflectance under controlled illumination, and the second computes physically based material parameters.

Polarized Image Capture To capture polarized image, we first perform system calibration that covers lighting, camera, and color calibration to ensure accurate lighting directions, view geometry, and consistent color response across all cameras for the subsequent optimization. The change in lighting polarization states is achieved by selectively activating different light sources on the light board. Each board adopts a hexagonal LED layout with alternating cross- and parallel-oriented polarizers in front of adjacent lights. This design enables capture of two complementary polarized images per illumination direction: cross-polarized (I_{\perp}) and parallel-polarized (I_{\parallel}) as shown in Fig. 1.

In theory, placing linear polarizers in front of light sources and analyzers with varying orientations before the camera enables the separation of diffuse and specular reflections. The intensity follows Malus’s Law: $I = I_0 \cos^2 \theta$, where θ denotes the angle between the transmission axes of the polarizer and analyzer. Since the mean value of $\cos^2 \theta$ over all orientations is $\frac{1}{2}$, the diffuse and specular radiance components under identical illumination can be expressed as:

$$I_d = 2I_{\perp}, \quad I_s = 2I_{\parallel} - 2I_{\perp}, \quad (1)$$

During capture, each object is scanned under cross- and parallel-polarized OLAT illumination, producing image sequences for all 346 lighting directions in 8 views:

$$\Lambda_{\perp}^i = \{I_{\perp}^k\}_{k=0}^N, \quad \Lambda_{\parallel}^i = \{I_{\parallel}^k\}_{k=0}^N, \quad N = 346. \quad (2)$$

Material Processing We present each material using diffuse albedo ρ_d , specular albedo ρ_s , and surface normal n . From the polarized images, diffuse and specular reflection sequences are computed as:

$$\Lambda_d = 2\Lambda_{\perp}, \quad \Lambda_s = 2(\Lambda_{\parallel} - \Lambda_{\perp}). \quad (3)$$

Following Lambert’s cosine law, we obtain the diffusion reflection by

$$L_o = \frac{L_i(\omega_i \cdot n)(\omega_o \cdot n)d\Omega dA}{d\Omega_o(\omega_o \cdot n)dA_o} = \frac{L_i(\omega_i \cdot n)d\Omega dA}{d\Omega_o dA_o} \quad (4)$$

where L_i is the incident radiance from the light source and L_o denotes the observed radiance. For each pixel of aperture area dA_o , diffuse albedo ρ_d and surface normal n are solved by minimizing $L = \{\rho_d | n \cdot \omega_k \}_{k=0}^N - \Lambda_d$.

Dataset	Type	Real-World	Capture					Lighting		Reflection			
			Geometry	Albedo	Specular	Normal	Multiview	HDRI	OLAT	Polarization	diffuse only	specular only	mix
Objaverse [12]	Objects	X	✓	✓	✓	✓	✓	✓	X	✓	✓	✓	
Hypersim [33]	Indoor Scene	X	✓	✓	✓	✓	✓	✓	X	X	X	✓	
Interverse [45]	Indoor Scene	X	✓	✓	✓	✓	✓	✓	X	X	X	✓	
Multi Illumination[30]	Objects	✓	X	X	X	X	X	X	X	X	X	✓	
D. Luo et al [26]	Flat Surface	✓	X	✓	✓	✓	X	✓	X	X	X	✓	
OpenSVBRDF[28]	Flat Surface	✓	X	✓	✓	✓	X	✓	X	X	X	✓	
Ours	Objects	✓	✓	✓	✓	✓	✓	✓	✓	✓	✓	✓	

Table 1. **Comparison between Material and Lighting-related Datasets.** Ours is the first real-world dataset that provides both comprehensive lighting coverage, polarization and material attributes enabling direct supervision for Inverse Rendering and Relighting.

We then derive the specular albedo ρ_s via the following:

$$\rho_s = \int_{\Omega} R_s(\omega_i, \omega_o) d\omega_i \approx \frac{4\pi\kappa}{N} \sum_{k=0}^N \hat{I}_s^k, \quad (5)$$

where R_s represents the specular reflection function of the material. κ is a constant determined by light intensity and solid angle in the capture device.

This two-stage process yields polarization-separated, multiview reflectance fields with corresponding material parameters suitable for physically-based rendering and relighting.

3.3. Dataset Statistics

Our dataset comprises 218 objects scanned across 346 lighting directions, 2 lighting polarization status and 8 views, totaling over 1.2M high-dynamic-range images at 6K resolution. For each object, we provide the raw cross- and parallel-polarized image sequences, along with the computed reflectance maps. The scanned objects span a diverse range of real-world materials, including metals, plastics, ceramics, concrete, fabrics, leathers, organics, wood, and transparent or translucent materials such as glass and wax. We further highlight the differences of our data with the existing dataset in Table 1.

Lighting Augmentation Extending from the OLAT capture setup, our dataset supports the synthesis of arbitrary novel illuminations with corresponding diffuse and specular separation. Given any environmental lighting texture as an environment map, we project it onto a unit sphere aligned with the calibrated light directions. For each light source, we sample the surrounding pixels on the environment map and compute their average intensity to determine the weighting of that light. The final relit result is obtained by performing a weighted sum over all OLAT images using these computed weights. This approach enables infinite lighting augmentation while maintaining accurate diffuse and specular ground truth through polarized imaging.

4. Inverse and Forward Rendering Model

To evaluate the effectiveness of the constructed dataset, we utilize our dataset to train both inverse and forward neural

rendering models. Specifically, we treat both neural rendering as an image-to-image translation problem and finetune from RGB2X [40], an image decomposition and synthesis method pretrained on synthetic data. For both training, we employ Low-Rank Adaptation [17] to prevent catastrophic forgetting.

Inverse Rendering Network. We design two types of inverse rendering models that produce decomposed intrinsic information in Physically-based Rendering (PBR) representation and Polarization representation.

Physically-based Rendering Workflow. Following the graphics convention, we design our decomposition network to predict physically meaningful material components, including diffuse albedo, specular albedo, and surface normal. The architecture is compatible with recent diffusion-based relighting frameworks, enabling seamless integration with existing pipelines.

Polarization Workflow. In addition to the traditional physically-based decomposition, we introduce a polarization-based workflow. The model decomposes the input into polarization components corresponding to cross-polarized and parallel-polarized images. Although diffuse and specular separation through polarization is not commonly available in standard imaging setups, polarization provides a powerful physical cue for reflection disentanglement. Specular reflections often disrupt multiview correspondences in 3D reconstruction due to their view-dependent nature, leading to geometry inconsistencies and reconstruction artifacts. By training a model to “virtualize” polarization, predicting cross- and parallel-polarized components from unpolarized inputs, we can recover diffuse and specular layers that facilitate more accurate relighting and benefit other challenging vision tasks that rely on precise reflectance modeling.

To control the diffusion model output in both workflows, we adopt a prompt-based conditioning mechanism: each target component (for example, “albedo” or “surface normal”) is encoded into a text embedding and injected into the diffusion model to guide the generation process.

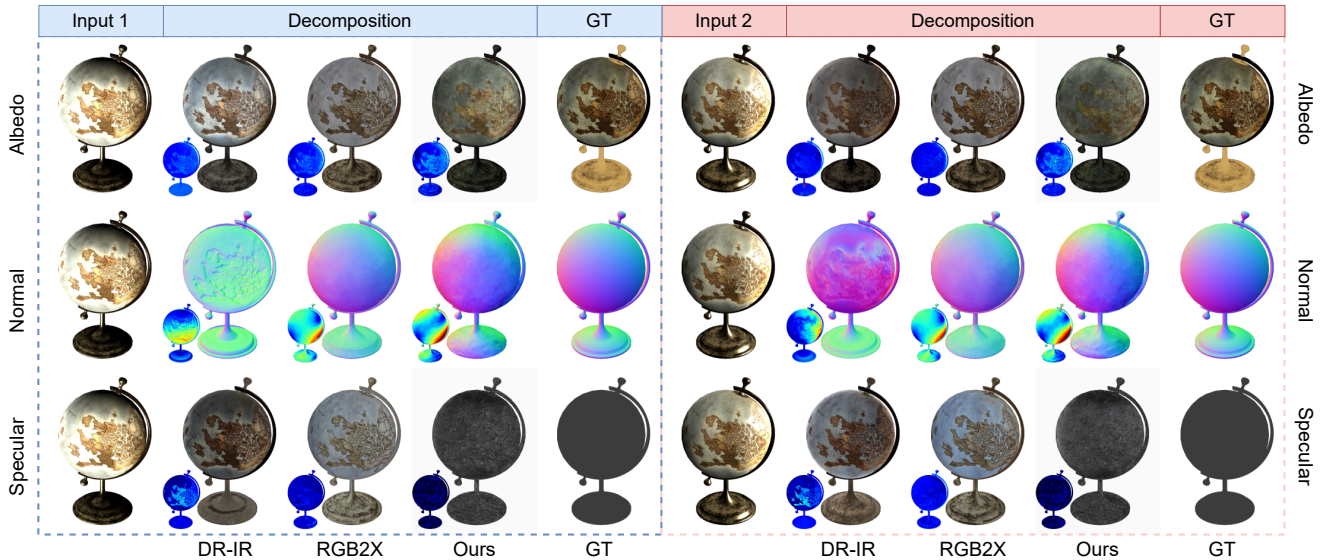


Figure 2. **Decomposition results on Objaverse samples.** Each row shows the predicted albedo, normal, and specular components from DR-IR, RGB2X, and ours under two lighting conditions. An error map is shown in the lower-left corner of each result. Post-training with our dataset produces more consistent decompositions and smoother material separation across illumination changes.

Baseline	Dataset	Albedo				Normal				Specular			
		MSE	PSNR	SSIM	LPIPS	MSE	PSNR	SSIM	LPIPS	MSE	PSNR	SSIM	LPIPS
HDRI Lighting													
lotus-D [16]	lightstage	–	–	–	–	0.010	24.722	0.767	0.398	–	–	–	–
dsine [1]	lightstage	–	–	–	–	0.008	25.509	0.776	0.401	–	–	–	–
DR [24]	lightstage	0.035	20.011	0.807	0.404	0.024	20.484	0.663	0.623	0.041	22.614	0.846	0.362
rgb2x [40]	lightstage	0.040	18.075	0.812	0.466	0.037	18.576	0.679	0.702	0.047	17.210	0.791	0.495
ours	lightstage	0.005	33.509	0.935	0.198	0.005	28.086	0.698	0.400	0.002	31.016	0.775	0.338
DR [24]	Objaverse	0.048	23.206	0.855	0.255	0.018	25.096	0.895	0.306	0.191	15.106	0.868	0.274
rgb2x [40]	Objaverse	0.042	22.882	0.888	0.333	0.008	28.825	0.886	0.358	0.052	20.278	0.860	0.451
ours	Objaverse	0.032	26.691	0.899	0.289	0.012	26.971	0.904	0.305	0.177	15.181	0.733	0.497
One-Light-at-a-Time (OLAT) Lighting													
lotus-D [16]	lightstage	–	–	–	–	0.019	20.914	0.771	0.500	–	–	–	–
dsine [1]	lightstage	–	–	–	–	0.021	21.220	0.764	0.489	–	–	–	–
DR [24]	lightstage	0.030	20.264	0.778	0.450	0.020	21.084	0.634	0.608	0.024	26.593	0.842	0.360
rgb2x [40]	lightstage	0.050	16.957	0.757	0.525	0.022	20.345	0.690	0.574	0.059	16.334	0.782	0.491
ours	lightstage	0.017	23.844	0.737	0.460	0.009	25.206	0.637	0.597	0.011	24.544	0.659	0.509
DR [24]	Objaverse	0.029	25.470	0.812	0.298	0.018	25.087	0.839	0.364	0.165	16.009	0.914	0.180
rgb2x [40]	Objaverse	0.021	25.162	0.657	0.578	0.012	26.971	0.904	0.305	0.081	18.247	0.715	0.623
ours	Objaverse	0.040	25.914	0.929	0.264	0.010	27.685	0.600	0.347	0.169	15.361	0.696	0.507

Table 2. Benchmarking decomposition under HDRI and OLAT lighting. Each lighting type is shown in a separate block for clarity.

Forward Rendering Network. We additionally train a forward rendering network with our dataset to render images from the intrinsic components, represented in either physically-based rendering (PBR) or polarization format. To explicitly model light interaction, we introduce an additional irradiance map computed as the integrated $\sum(n \cdot \omega)$ over all sampled light directions weighted by the corre-

sponding light source color.

During training, we employ lighting augmentation that combines three types of input images: (1) real captures under one-light-at-a-time (OLAT) illumination, (2) synthesized HDRI lighting generated via weighted summation of OLAT images using environment-map-based light weights (Sec. 3.3), and (3) direct captures under all-white illumina-

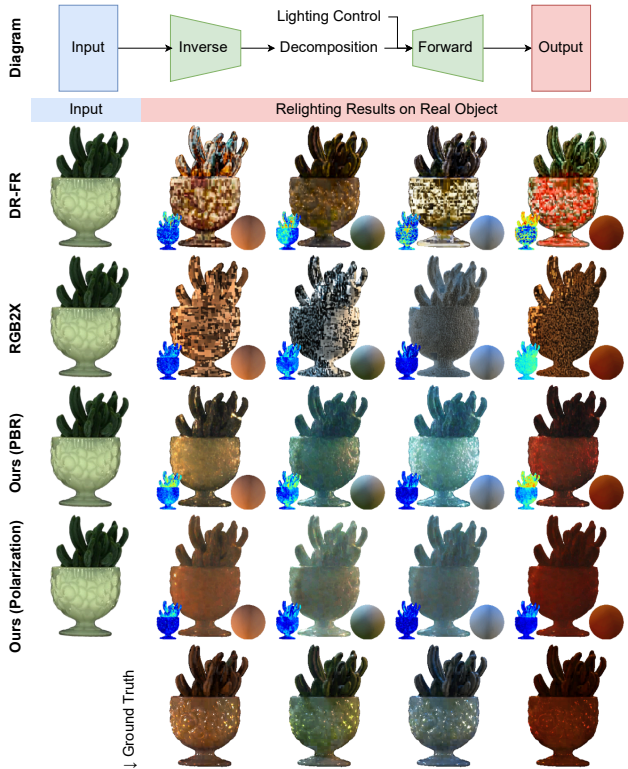


Figure 3. **Forward relighting results on real objects (Light Stage dataset) under HDRI lighting** Each row shows the relighting outputs from DR-FR, RGB2X, and our model under both the PBR and polarization workflows. The top diagram illustrates the full inverse-to-forward relighting pipeline. For each relit result, the error map is shown in the lower-left corner and the lighting reference in the lower-right corner.

tion. For each training sample, we randomly select an object’s intrinsic material components, including diffuse albedo, surface normal in camera space, and specular albedo from an arbitrary camera view, and pair them with the associated irradiance map as inputs. The text prompt is left empty, and supervision is applied through an L2 loss with respect to the target image under the corresponding augmented lighting condition.

5. Evaluation and Experiments

5.1. Setup

Baselines Lotus [16] introduces a simple yet effective adaptation protocol for dense prediction tasks, enabling zero-shot depth and normal estimation. RGB2X [40] and Diffusion Renderer [24] are two recent material decomposition and relighting methods, trained on synthetic data, that are direct baselines to us. We additionally include Dsine [1], an off-the-shelf normal estimator also trained exclusively on synthetic data.

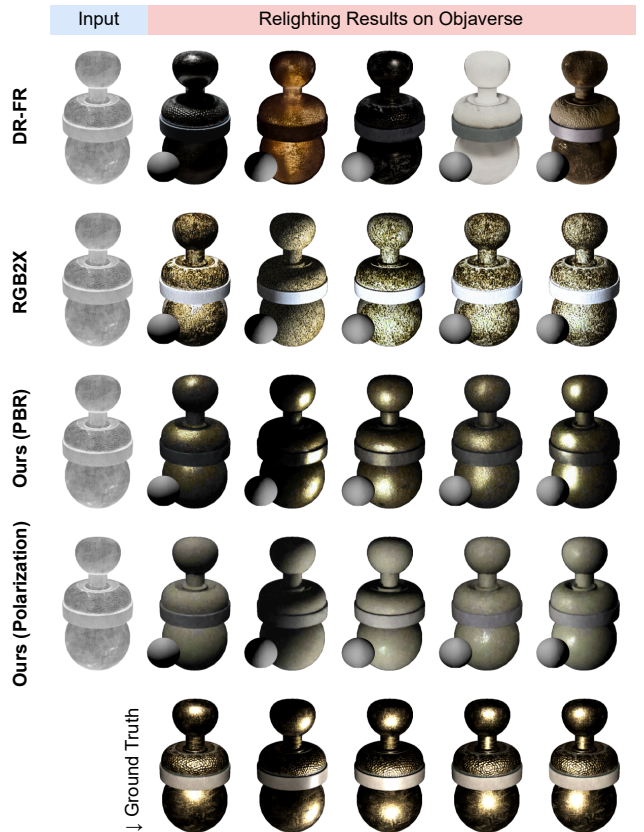


Figure 4. **Forward relighting results on the Objaverse dataset under OLAT lighting.** The lighting reference is shown in the lower-left corner.

Synthetic Dataset For evaluation, we curated a subset of 50 objects from the Objaverse Dataset [12] and rendered their material components—base color, surface normals, and specular maps—using the Blender Eevee rendering engine[5]. For each object, we generated 60 turntable views uniformly spaced across 360 degrees. To simulate OLAT-style lighting, we additionally rendered all 346 individual lighting directions per view. Each lighting direction was represented by a custom HDRI environment map constructed using a single hexagonal area light, spatially positioned and oriented to match the corresponding LED in the original Light Stage configuration.

5.2. Evaluation

Decomposition We evaluate the effectiveness of our material dataset for inverse decomposition, the task of decomposing an input RGB image into its intrinsic physical components: diffuse albedo, surface normal, and specular albedo. RGB2X and Diffusion Renderer Inverse (DR-IR) are benchmarked on our dataset and the synthetic Objaverse dataset (Sec. 5.1). Lotus-D and Dsine are included for comparison on surface-normal prediction only. Two in-

Input Lighting		HDRI				OLAT			
Baseline	dataset	MSE	PSNR	SSIM	LPIPS	MSE	PSNR	SSIM	LPIPS
DR[24]	lightstage	0.058	16.972	0.775	0.386	0.020	23.565	0.798	0.335
rgb2x[40]	lightstage	0.038	18.495	0.514	0.514	0.046	17.529	0.475	0.559
ours-GBuffer	lightstage	0.005	27.798	0.904	0.211	0.011	24.850	0.850	0.301
ours-Polarization	lightstage	0.007	26.133	0.909	0.200	0.010	25.331	0.802	0.388
DR[24]	Objaverse	0.066	20.934	0.754	0.517	0.026	25.092	0.873	0.229
rgb2x[40]	Objaverse	0.032	24.386	0.595	0.606	0.014	26.861	0.598	0.547
ours-GBuffer	Objaverse	0.014	26.762	0.956	0.103	0.014	27.638	0.932	0.203
ours-Polarization	Objaverse	0.007	29.554	0.964	0.093	0.021	25.689	0.914	0.249

Table 3. Evaluation on relighting.

Input Settings	Raw Images				Pred Diffuse Images				Pred Albedo Images			
	MSE	PSNR	SSIM	LPIPS	MSE	PSNR	SSIM	LPIPS	MSE	PSNR	SSIM	LPIPS
Dust3r	0.102	14.512	0.226	0.604	0.060	17.783	0.411	0.556	0.054	20.302	0.513	0.506
Mast3r	0.161	12.719	0.193	0.613	0.132	13.777	0.247	0.615	0.130	15.565	0.282	0.603

Table 4. **Sparse-view 3D reconstruction on 50 real-world objects (8-view input).** We compare four input settings: raw, polarized diffuse, predicted diffuse (polarization workflow), and predicted albedo (PBR workflow). Both methods are evaluated with and without masking. The best score in each row across settings is highlighted in bold.

put lighting setups are considered: **1) HDRI lighting**, rendered directly for synthetic data and synthesized for our Light Stage dataset by linearly combining OLAT captures using weights derived from the lighting augmentation module; and **2) OLAT lighting**, where synthetic data are rendered with the prepared 346 OLAT HDRIs (Sec. 5.1) and real data use the captured OLAT images directly. RGB2X is further post-trained on our dataset to evaluate real-world adaptation.

Figure 2 presents qualitative decompositions under different lighting setups. Table 2 summarizes quantitative metrics across 50 objects from our dataset and 50 objects from Objaverse based on four metrics for visual similarity: MSE, PSNR, SSIM and LPIPS [41]. Under **HDRI lighting**, our model markedly improves decomposition accuracy. These gains highlight the benefit of real-world polarization cues for disentangling diffuse and geometric components under complex illumination. Under **OLAT lighting**, where inputs are illuminated by calibrated directional HDRIs, our model also achieves the lowest overall MSE and highest PSNR, confirming robustness to directional illumination. The improvement on specular is less evident, partly because specular reflectance is defined inconsistently across rendering engines—some model it via index of refraction or roughness, whereas our dataset measures it through polarization-based separation, resulting in a different normalization. Despite the smaller numerical gain, qualitative results show clearer highlight separation.

Relighting We further evaluate the effectiveness of our polarized reflectance dataset for relighting, where the goal is to render from decomposed material components under novel illumination settings. Two workflows are examined:

1) the PBR workflow, which uses diffuse albedo and surface normal for physically based shading, and **2) the polarization workflow**, which leverages polarization-separated components to model diffuse-specular interactions. To guide the relighting, we additionally provide an irradiance map computed as the integrated $\sum(n \cdot \omega)$ over all sampled light directions weighted by its color.

We benchmark RGB2X and Diffusion Renderer on both our Light Stage and Objaverse datasets under HDRI and OLAT lighting. RGB2X is further post-trained on our dataset to assess adaptation to real-world reflectance.

Figure 3 and Figure 4 visualize the relighting results on both datasets. Quantitative comparisons are reported in Table 3, following the same evaluation scale as the decomposition evaluation. For each lighting setup, we report both PBR and polarization workflows to analyze the influence of physical supervision.

In the **PBR workflow**, our relighting model produces markedly improved shading continuity and global color balance. On real Light Stage objects, shadows align more faithfully with geometry, and highlight energy remains stable across lighting directions. Quantitatively, PSNR increases from 18.5 dB to 27.8 dB and SSIM from 0.51 to 0.90, confirming that real polarization-aligned data help the network learn a smoother irradiance response. Compared to DR-FR, which tends to overfit synthetic radiance distributions, the post-trained model generalizes better to real illumination, maintaining global color balance and shading smoothness.

In the **polarization workflow**, relighting results demonstrate stronger lighting consistency and reduced noise in glossy regions. The polarization-based supervision constrains diffuse-specular interaction and mitigates cross-

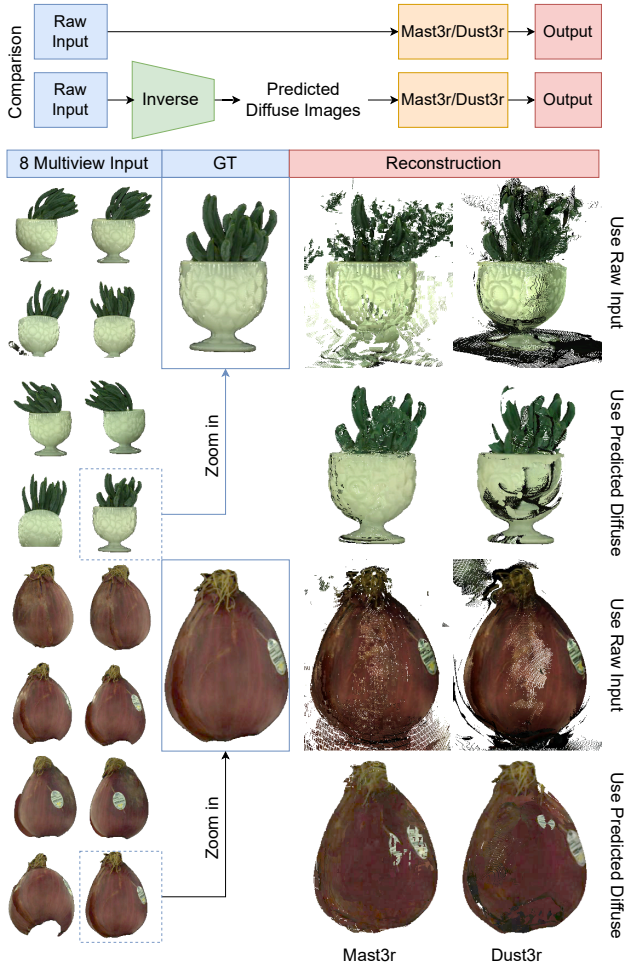


Figure 5. **Impact of our inverse model on sparse-view 3D reconstruction.** We compare reconstructions from Dust3r and Mast3r using raw input images and our predicted diffuse images from the inverse decomposition model. The reconstruction takes 8 sparse multiview input.

polarization artifacts, yielding more stable illumination transitions on real captures. However, the visual quality on synthetic examples is slightly lower than the PBR workflow—an expected outcome given the domain gap between polarization-separated captures and renderer-generated materials. Despite this, the polarization workflow maintains high physical consistency and perceptual alignment, with LPIPS = 0.200 indicating faithful reconstruction of lighting effects.

Sparse 3D Reconstruction Sparse-view 3D reconstruction is highly sensitive to view-dependent specularities that violate the Lambertian assumption, often leading to inconsistent geometry and photometric errors. Polarization helps address this issue by physically separating diffuse and specular components, enabling cleaner multiview correspon-

dences. However, in real-world scenarios, polarized images are rarely available. With our dataset and proposed polarization workflow, once an inverse model is trained with polarized supervision, it can predict polarization-equivalent outputs, such as diffuse-like images, from standard unpolarized inputs.

Figure 5 visualizes how the trained inverse model can help with sparse view reconstruction methods. We showcase the improvement using Dust3r [37] and Mast3r [37], and present quantitative comparisons in Table 4.

We evaluate three settings, all based on the same 8-view captures on 50 randomly selected objects: (1) using the raw images as input, (2) using diffuse-only images generated by our pretrained inverse model through the polarization workflow, and (3) using diffuse albedo generated by our pretrained inverse model through the PBR workflow as input. The differences among these experimental settings are illustrated in the top diagram of Figure 5. Both Dust3r and Mast3r reconstruct 3D geometry and reproject the recovered points into image space to compute reconstruction errors, summarized in Table 4.

Across these configurations, we also report masked results following [19]. The predicted albedo images from our inverse model (setting 3) achieve the highest image-based reconstruction metrics, followed by the predicted diffuse images (setting 2). When masking is applied, the reconstruction performance with predicted diffuse images improves further. These findings highlight that, once trained, the inverse model effectively generates normalized, specular-free multiview images suitable for downstream 3D reconstruction. Moreover, the inherent denoising process of the diffusion model contributes to smoother and more consistent reconstructions, the predicted diffuse images even achieve higher PSNR values than the captured diffuse images.

6. Conclusion and Limitation

We introduced the large-scale polarized reflection and material dataset of real-world objects at scale, providing dense diffuse–specular separation and material attributes across 200+ objects, 346 lighting directions, and 8 calibrated views. Experiments show that models trained on our measurements achieve substantially improved intrinsic decomposition, relighting quality, and multiview consistency compared to synthetic-only baselines. **Limitations.** Our capture setup is constrained to static objects within a controlled Light Stage, making highly transparent, dynamic, or strongly anisotropic materials difficult to measure. The dataset does not capture subsurface parameters. Future work will extend the capture to more complex materials and explore scalable, in-the-wild acquisition.

References

- [1] Gwangbin Bae and Andrew J. Davison. Rethinking inductive biases for surface normal estimation. In *IEEE/CVF Conference on Computer Vision and Pattern Recognition (CVPR)*, 2024. 5, 6
- [2] Harry Barrow, J Tenenbaum, A Hanson, and E Riseman. Recovering intrinsic scene characteristics. *Comput. vis. syst.*, 2(3-26):2, 1978. 1, 2
- [3] Sean Bell, Kavita Bala, and Noah Snavely. Intrinsic images in the wild. *ACM Transactions on Graphics (TOG)*, 33(4):1–12, 2014. 2
- [4] Anand Bhattad, Daniel McKee, Derek Hoiem, and David A. Forsyth. Stylegan knows normal, depth, albedo, and more. *arXiv preprint arXiv:2301.04638*, 2023. 2
- [5] Blender Online Community. Blender - a 3d modelling and rendering package. <https://www.blender.org>, 2024. 6
- [6] Mark Boss, Varun Jampani, Kihwan Kim, Hendrik Lensch, and Jan Kautz. Two-shot spatially-varying brdf and shape estimation. In *Proceedings of the IEEE/CVF Conference on Computer Vision and Pattern Recognition*, pages 3982–3991, 2020. 2
- [7] Chris Careaga and Yağız Aksoy. Intrinsic image decomposition via ordinal shading. *ACM Transactions on Graphics*, 43(1):1–24, 2023. 2
- [8] Qifeng Chen and Vladlen Koltun. A simple model for intrinsic image decomposition with depth cues. In *Proceedings of the IEEE international conference on computer vision*, pages 241–248, 2013. 1, 2
- [9] Zhifei Chen, Tianshuo Xu, Wenhong Ge, Leyi Wu, Dongyu Yan, Jing He, Luozhou Wang, Lu Zeng, Shunsi Zhang, and Ying-Cong Chen. Uni-renderer: Unifying rendering and inverse rendering via dual stream diffusion. In *Proceedings of the Computer Vision and Pattern Recognition Conference*, pages 26504–26513, 2025. 1, 2
- [10] Changwoon Choi, Juhyeon Kim, and Young Min Kim. Iblnerf: Image-based lighting formulation of neural radiance fields. In *Computer Graphics Forum*, page e14929. Wiley Online Library, 2023. 2
- [11] JunYong Choi, Min-cheol Sagong, SeokYeong Lee, Seung-Won Jung, Ig-Jae Kim, and Junghyun Cho. Channel-wise noise scheduled diffusion for inverse rendering in indoor scenes. In *Proceedings of the Computer Vision and Pattern Recognition Conference*, pages 5773–5782, 2025. 1, 2
- [12] Matt Deitke, Dustin Schwenk, Jordi Salvador, Luca Weihs, Oscar Michel, Eli VanderBilt, Ludwig Schmidt, Kiana Ehsani, Aniruddha Kembhavi, and Ali Farhadi. Objaverse: A universe of annotated 3d objects. *arXiv preprint arXiv:2212.08051*, 2022. 1, 3, 4, 6
- [13] Matt Deitke, Ruoshi Liu, Matthew Wallingford, Huong Ngo, Oscar Michel, Aditya Kusupati, Alan Fan, Christian Laforte, Vikram Voleti, Samir Yitzhak Gadre, Eli VanderBilt, Aniruddha Kembhavi, Carl Vondrick, Georgia Gkioxari, Kiana Ehsani, Ludwig Schmidt, and Ali Farhadi. Objaverse-xl: A universe of 10m+ 3d objects. *arXiv preprint arXiv:2307.05663*, 2023. 3
- [14] Qingnan Fan, Jiaolong Yang, Gang Hua, Baoquan Chen, and David Wipf. Revisiting deep intrinsic image decompositions. In *Proceedings of the IEEE conference on computer vision and pattern recognition*, pages 8944–8952, 2018. 2
- [15] Elena Garces, Adolfo Munoz, Jorge Lopez-Moreno, and Diego Gutierrez. Intrinsic images by clustering. In *Computer graphics forum*, pages 1415–1424. Wiley Online Library, 2012. 1, 2
- [16] Jing He, Haodong Li, Wei Yin, Yixun Liang, Leheng Li, Kaiqiang Zhou, Hongbo Zhang, Bingbing Liu, and Ying-Cong Chen. Lotus: Diffusion-based visual foundation model for high-quality dense prediction. In *The Thirteenth International Conference on Learning Representations*, 2025. 2, 5, 6
- [17] Edward J Hu, Yelong Shen, Phillip Wallis, Zeyuan Allen-Zhu, Yuanzhi Li, Shean Wang, Lu Wang, Weizhu Chen, et al. Lora: Low-rank adaptation of large language models. *ICLR*, 1(2):3, 2022. 4
- [18] Bingxin Ke, Kevin Qu, Tianfu Wang, Nando Metzger, Shengyu Huang, Bo Li, Anton Obukhov, and Konrad Schindler. Marigold: Affordable adaptation of diffusion-based image generators for image analysis, 2025. 2
- [19] Alexander Kirillov, Eric Mintun, Nikhila Ravi, Hanzi Mao, Chloe Rolland, Laura Gustafson, Tete Xiao, Spencer Whitehead, Alexander C Berg, Wan-Yen Lo, et al. Segment anything. In *Proceedings of the IEEE/CVF international conference on computer vision*, pages 4015–4026, 2023. 8
- [20] Wenbin Li, Sajad Saeedi, John McCormac, Ronald Clark, Dimos Tzoumanikas, Qing Ye, Yuzhong Huang, Rui Tang, and Stefan Leutenegger. Interiornet: Mega-scale multi-sensor photo-realistic indoor scenes dataset. *arXiv preprint arXiv:1809.00716*, 2018. 3
- [21] Zhengqi Li and Noah Snavely. Cgintrinsics: Better intrinsic image decomposition through physically-based rendering. In *Proceedings of the European Conference on Computer Vision (ECCV)*, pages 371–387, 2018. 1, 2, 3
- [22] Zhengqin Li, Mohammad Shafiei, Ravi Ramamoorthi, Kalyan Sunkavalli, and Manmohan Chandraker. Inverse rendering for complex indoor scenes: Shape, spatially-varying lighting and svbrdf from a single image. In *Proceedings of the IEEE/CVF conference on computer vision and pattern recognition*, pages 2475–2484, 2020. 3
- [23] Zhengqin Li, Ting-Wei Yu, Shen Sang, Sarah Wang, Meng Song, Yuhan Liu, Yu-Ying Yeh, Rui Zhu, Nitesh Gundavarapu, Jia Shi, et al. Openrooms: An open framework for photorealistic indoor scene datasets. In *Proceedings of the IEEE/CVF conference on computer vision and pattern recognition*, pages 7190–7199, 2021. 1, 3
- [24] Ruofan Liang, Zan Gojcic, Huan Ling, Jacob Munkberg, Jon Hasselgren, Chih-Hao Lin, Jun Gao, Alexander Keller, Nandita Vijaykumar, Sanja Fidler, et al. Diffusion renderer: Neural inverse and forward rendering with video diffusion models. In *Proceedings of the Computer Vision and Pattern Recognition Conference*, pages 26069–26080, 2025. 1, 2, 5, 6, 7
- [25] Isabella Liu, Linghao Chen, Ziyang Fu, Liwen Wu, Haiyan Jin, Zhong Li, Chin Ming Ryan Wong, Yi Xu, Ravi Ramamoorthi, Zexiang Xu, and Hao Su. Openillumination:

- A multi-illumination dataset for inverse rendering evaluation on real objects, 2024. [3](#)
- [26] Di Luo, Hanxiao Sun, Lei Ma, Jian Yang, and Beibei Wang. Correlation-aware encoder-decoder with adapters for svbrdf acquisition. In *Proceedings of SIGGRAPH Asia 2024*, 2024. [4](#)
- [27] Jundan Luo, Duygu Ceylan, Jae Shin Yoon, Nanxuan Zhao, Julien Philip, Anna Frühstück, Wenbin Li, Christian Richardt, and Tuanfeng Wang. Intrinsicdiffusion: Joint intrinsic layers from latent diffusion models. In *ACM SIGGRAPH 2024 Conference Papers*, pages 1–11, 2024. [1](#), [2](#)
- [28] Xiaohe Ma, Xianmin Xu, Leyao Zhang, Kun Zhou, and Hongzhi Wu. Opensvbrdf: A database of measured spatially-varying reflectance. *ACM Trans. Graph.*, 42(6), 2023. [3](#), [4](#)
- [29] Abhimitra Meka, Mohammad Shafiei, Michael Zollhöfer, Christian Richardt, and Christian Theobalt. Real-time global illumination decomposition of videos. *ACM Transactions on Graphics (ToG)*, 40(3):1–16, 2021. [2](#)
- [30] Lukas Murmann, Michael Gharbi, Miika Aittala, and Fredo Durand. A dataset of multi-illumination images in the wild. In *Proceedings of the IEEE/CVF International Conference on Computer Vision*, pages 4080–4089, 2019. [1](#), [3](#), [4](#)
- [31] Takuya Narihira, Michael Maire, and Stella X Yu. Direct intrinsics: Learning albedo-shading decomposition by convolutional regression. In *Proceedings of the IEEE international conference on computer vision*, pages 2992–2992, 2015. [2](#)
- [32] Ravi Ramamoorthi and Pat Hanrahan. A signal-processing framework for inverse rendering. In *Proceedings of the 28th annual conference on Computer graphics and interactive techniques*, pages 117–128, 2001. [1](#)
- [33] Mike Roberts, Jason Ramapuram, Anurag Ranjan, Atulit Kumar, Miguel Angel Bautista, Nathan Paczan, Russ Webb, and Joshua M Susskind. Hypersim: A photorealistic synthetic dataset for holistic indoor scene understanding. In *Proceedings of the IEEE/CVF international conference on computer vision*, pages 10912–10922, 2021. [1](#), [3](#), [4](#)
- [34] Carsten Rother, Martin Kiefel, Lumin Zhang, Bernhard Schölkopf, and Peter Gehler. Recovering intrinsic images with a global sparsity prior on reflectance. *Advances in neural information processing systems*, 24, 2011. [1](#), [2](#)
- [35] Jian Shi, Yue Dong, Hao Su, and Stella X Yu. Learning non-lambertian object intrinsics across shapenet categories. In *Proceedings of the IEEE conference on computer vision and pattern recognition*, pages 1685–1694, 2017. [2](#)
- [36] Shanlin Sun, Yifan Wang, Hanwen Zhang, Yifeng Xiong, Qin Ren, Ruogu Fang, Xiaohui Xie, and Chenyu You. Ouroboros: Single-step diffusion models for cycle-consistent forward and inverse rendering. In *Proceedings of the IEEE/CVF International Conference on Computer Vision*, pages 10386–10397, 2025. [1](#), [2](#)
- [37] Shuzhe Wang, Vincent Leroy, Yohann Cabon, Boris Chidlovskii, and Jerome Revaud. Dust3r: Geometric 3d vision made easy. In *CVPR*, 2024. [8](#)
- [38] Zian Wang, Jonah Philion, Sanja Fidler, and Jan Kautz. Learning indoor inverse rendering with 3d spatially-varying lighting. In *Proceedings of the IEEE/CVF International Conference on Computer Vision*, pages 12538–12547, 2021. [2](#)
- [39] Felix Wimbauer, Shangzhe Wu, and Christian Rupprecht. De-rendering 3d objects in the wild. In *Proceedings of the IEEE/CVF Conference on Computer Vision and Pattern Recognition*, pages 18490–18499, 2022. [2](#)
- [40] Zhixin Zeng, Valentin Deschaintre, Iliyan Georgiev, Yannick Hold-Geoffroy, Yuanming Hu, Fujun Luan, Ling-Qi Yan, and Miloš Hašan. Rgbx: Image decomposition and synthesis using material- and lighting-aware diffusion models. In *ACM SIGGRAPH 2024 Conference Proceedings*, New York, NY, USA, 2024. Association for Computing Machinery. [1](#), [2](#), [4](#), [5](#), [6](#), [7](#)
- [41] Richard Zhang, Phillip Isola, Alexei A Efros, Eli Shechtman, and Oliver Wang. The unreasonable effectiveness of deep features as a perceptual metric. In *Proceedings of the IEEE conference on computer vision and pattern recognition*, pages 586–595, 2018. [7](#)
- [42] Qi Zhao, Ping Tan, Qiang Dai, Li Shen, Enhua Wu, and Stephen Lin. A closed-form solution to retinex with non-local texture constraints. *IEEE transactions on pattern analysis and machine intelligence*, 34(7):1437–1444, 2012. [1](#), [2](#)
- [43] Rongjia Zheng, Qing Zhang, Chengjiang Long, and Wei-Shi Zheng. Dnf-intrinsic: Deterministic noise-free diffusion for indoor inverse rendering. In *Proceedings of the IEEE/CVF International Conference on Computer Vision*, pages 10342–10352, 2025. [1](#), [2](#)
- [44] Tinghui Zhou, Philipp Krahenbuhl, and Alexei A Efros. Learning data-driven reflectance priors for intrinsic image decomposition. In *Proceedings of the IEEE international conference on computer vision*, pages 3469–3477, 2015. [2](#)
- [45] Jingsen Zhu, Fujun Luan, Yuchi Huo, Zihao Lin, Zhihua Zhong, Dianbing Xi, Rui Wang, Hujun Bao, Jiayang Zheng, and Rui Tang. Learning-based inverse rendering of complex indoor scenes with differentiable monte carlo raytracing. In *SIGGRAPH Asia 2022 Conference Papers*. ACM, 2022. [4](#)